Wavefront sensing and control for a Photonic Lantern Nuller for exoplanet characterization

Yinzi Xin[a], Daniel Echeverri[a], Nemanja Jovanovic[a], Dimitri Mawet[a,b], Sergio Leon-Saval[c], Rodrigo Amezcua-Correa[d], Stephanos Yerolatsitis[d], Michael P. Fitzgerald[e], Pradip Gatkine[a], Yoo Jung Kim[e], Jonathan Lin[e], Barnaby Norris[f], Garreth Ruane[b], and Steph Sallum[g]

[a]Department of Astronomy, California Institute of Technology, 1200 E California Blvd, Pasadena, CA, 91125, USA
[b]Jet Propulsion Laboratory, California Institute of Technology, 4800 Oak Grove Drive, Pasadena, CA, 91109, USA
[c]Sydney Astrophotonic Instrumentation Laboratory, School of Physics, The University of Sydney, Sydney, NSW 2006, Australia
[d]The College of Optics and Photonics, University of Central Florida, 4304 Scorpius St, Orlando, FL 32816
[e]Department of Physics & Astronomy, 430 Portola Plaza, University of California, Los Angeles, CA 90095, USA
[f]Sydney Institute for Astronomy, School of Physics, Physics Road, The University of Sydney, NSW 2006, Australia
[g]Department of Physics & Astronomy, University of California, Irvine, 4129 Frederick Reines Hall, Irvine, CA 92697 USA

ABSTRACT

Coronagraphs allow for faint off-axis exoplanets to be observed, but are limited to angular separations greater than a few beam widths. Accessing closer-in separations would greatly increase the expected number of detectable planets, which scales inversely with the inner working angle. The Photonic Lantern Nuller (PLN) is an instrument concept designed to characterize exoplanets within a single beam-width of its host star, using a device called the mode-selective photonic lantern (MSPL), a photonic mode-converter that maps linearly polarized modes into individual single-mode outputs. The PLN leverages the spatial symmetry of an MSPL to create nulled ports, which cancel out on-axis starlight but allow off-axis exoplanet light to couple. The null-depths are limited by wavefront aberrations in the system as well as by imperfections in the lantern's response. However, wavefront sensing and control can be used to improve the null-depths achievable. We extend the technique of Implicit Electric Field Conjugation, commonly used to create dark zones with coronagraphic instruments, to work with a PLN. We present results from simulations and from in-lab testbed experiments.

Keywords: photonic lanterns, astrophotonics, nulling interferometry, wavefront control, implicit electric field conjugation

1. INTRODUCTION

The characterization of exoplanets was identified by the Decadal Survey for Astronomy and Astrophysics 2020 as one of the top scientific priorities.[1] High-resolution spectroscopy is especially critical for many measurements, including that of the planet's radial velocity, spin, atmospheric composition, and surface features through Doppler imaging.[2] It can also enable the potential detection of exomoons.[3] The Photonic Lantern Nuller[4,5] is an instrument concept that enables the high-resolution spectral characterization of exoplanets at and within 1 λ/D,

Further author information: (Send correspondence to Y.X)
Y.X: E-mail: yxin@caltech.edu

Optical and Infrared Interferometry and Imaging IX, edited by Jens Kammerer, Stephanie Sallum, Joel Sanchez-Bermudez, Proc. of SPIE Vol. 13095, 130950S
 · 0277-786X · doi: 10.1117/12.3019168

where λ is the wavelength and D the telescope diameter. It is inspired by the Vortex Fiber Nuller (VFN),[6,7] but unlike the VFN, which has only one nulled channel with a circularly symmetric coupling profile, the PLN provides four nulled channels, each with a unique coupling profile. This allows for more planet flux to be retained, and also helps place better constraints on the planet's flux ratio and spatial position.[4]

The PLN exploits the symmetries of the ports of a six port mode-selective photonic lantern (MSPL),[8] a special type of photonic lantern[9] that utilizes dissimilar cores that enable ports to be mapped into linearly polarized (LP) modes, or the eigenmodes of a radially symmetric, weakly guiding step-index waveguide. Each mode at the multi-mode face (MMF) of the lantern is mapped to a single-mode fiber (SMF) output, such that light coupling to a given mode at the MMF side will result in flux in the corresponding SMF core. The symmetries of the modes corresponding to the MSPL ports results in a null at the center (to which the star is aligned), with finite transmission off-axis where potential planets may exist.

The operating principles of the PLN are fully derived in Ref. 4, and the first laboratory demonstration of the PLN (in both monochromatic and broadband light) is presented in Ref. 10. In this work, we present the results of using wavefront control — specifically the implicit electric field conjugation algorithm (iEFC)[11] — to deepen the central nulls of the PLN.

2. IMPLICIT ELECTRIC FIELD CONJUGATION

The implicit electric field conjugation algorithm for active suppression of starlight is described in Ref 11. We present a simplified overview of it here.

The stellar electric field can be modulated by applying probes on the deformable mirror (DM), and the electric field is linearly related to the difference between an image with some probe and the image with the same probe but with opposite sign. Minimizing the measurement δ — a series of such 'differenced' images — thus also minimizes the electric field. We can empirically calibrate the influence of the DM on δ by applying a mode on the DM and encoding the change in δ that it produces into a response matrix:

$$\delta = S\alpha, \tag{1}$$

where α is the DM command and S the calibrated response matrix. The iEFC solution is given by

$$\alpha = \arg\min_{\alpha} |\delta + S\alpha|^2 + \lambda|\alpha|^2 = -(S^T S + \lambda I)^{-1} S^T \delta = -C\delta. \tag{2}$$

The parameter λ can be set to penalize large DM solutions, and the control matrix $C = (S^T S + \lambda I)^{-1} S^T$ is computed ahead of time, after calibrations are complete.

Unlike the alternative Electric Field Conjugation algorithm, which is model-based, iEFC is data-driven. It has the advantage of not being limited by model fidelity but also the disadvantage of requiring testbed calibration time. We choose to use iEFC, however, because it is *relatively* more advantageous for the PLN than for conventional coronagraphs, because the PLN only has four ports and thus requires significantly fewer modes to be calibrated.

For this work, we use the implementation of iEFC from the lina package.[12]

3. EXPERIMENTAL SETUP

A detailed schematic of the front-end of Polychromatic Reflective Testbed (PoRT) can be found in Ref. 10, along with the PLN coupling maps measured using the testbed without wavefront control — i.e. the DM merely flattened by maximizing coupling through a single-mode fiber. The results with the monochromatic laser injected using a polarization maintaining fiber are presented again in Figure 1. These coupling maps were obtained using a photodiode with only one input, and therefore had to be measured sequentially. However, for wavefront control, it is convenient to be able to measure the coupling through all the relevant ports simultaneously.

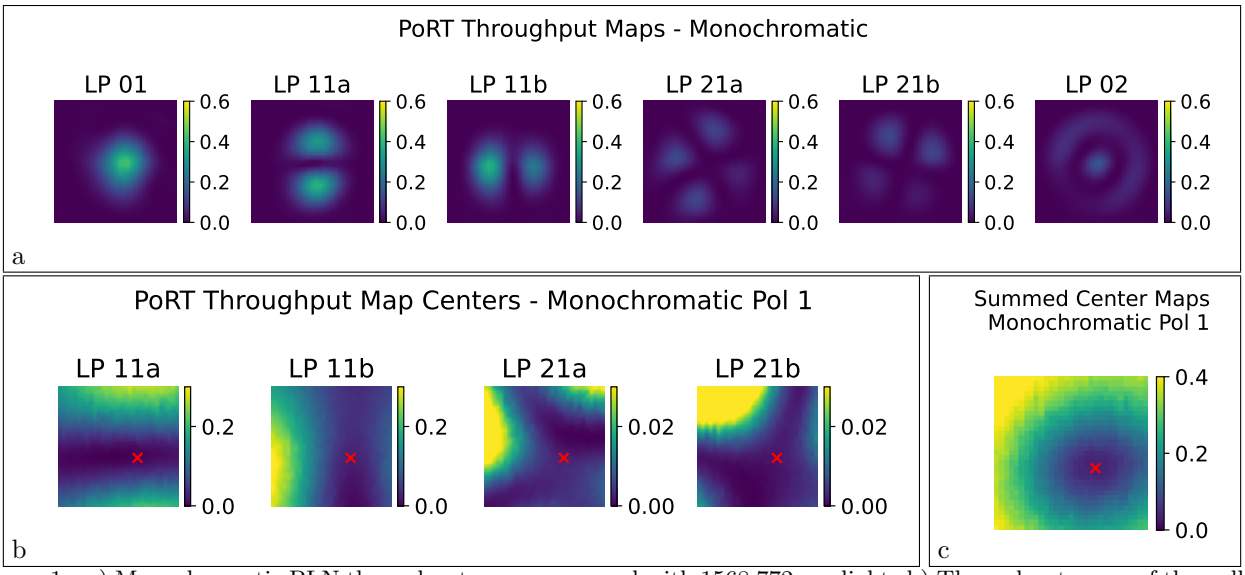

Figure 1. a) Monochromatic PLN throughput maps measured with 1568.772 nm light. b) Throughput maps of the nulled ports with fine spatial sampling of the center. The red crosses indicate the axial center of the lantern, identified using the map in part (c). c) The summed throughput of the four maps in part (b). The location of minimum summed throughput is taken to be the lantern center, where η_s is measured. Figure adapted from Ref. 10.

In Figure 2a, we present a updated simplified diagram of PoRT, which now includes a back-end that images the outputs of the nulled ports onto a camera, allowing the fluxes coupled into each port to be simultaneously measured using photometry. Figure 2b shows an example camera image, cropped to the region containing the lantern outputs and with the dark frame (the camera image when the light source is turned off) subtracted. The overlaid circles indicate the apertures used for photometry, where each intensity measurement is the sum of the counts contained within the defined circle. When the incoming beam is aligned to the 'center' of the lantern (which we choose as the location of minimum summed coupling as in Figure 1), these intensity measurements correspond to the stellar coupling through each port of the lantern. These intensity measurements are proportional to η_s, or the fraction of the incoming starlight coupled into each port. For closed-loop wavefront control, all four nulled ports are routed to the V-groove, and we work directly with the intensity measurements made on the camera (i.e. the sum of the counts in each aperture). We leave the non-nulled ports disconnected in order to not saturate the camera. After performing wavefront control, we use the photodiode to obtain normalized coupling maps sequentially for each port.

4. IMPLEMENTATION AND RESULTS

We define the following two sets of probes, where Z_n is the nth Noll-ordered Zernike mode defined across the 12×12 DM actuator grid, each with an RMS of 1:

$$p_{1_\pm} = \pm(Z_5 + Z_6 + Z_7 + Z_8)/\sqrt{4} \tag{3}$$

$$p_{2_\pm} = \pm(Z_5 - Z_6 + Z_7 - Z_8)/\sqrt{4} \tag{4}$$

Using a probe amplitude of 0.02 and a mode input amplitude of 0.01 (both in DM control units that range from 0 to 1), we then calibrate the response matrix S across the set of Zernikes modes from Z_4 to Z_{20} (a total of 17 modes). For our measurements, we divide the summed counts by 10^6 such that the measured responses are closer in scale to our control inputs. We then calculate the control matrix C using λ equal to 1/10 of the maximum diagonal value of $S^T S$.

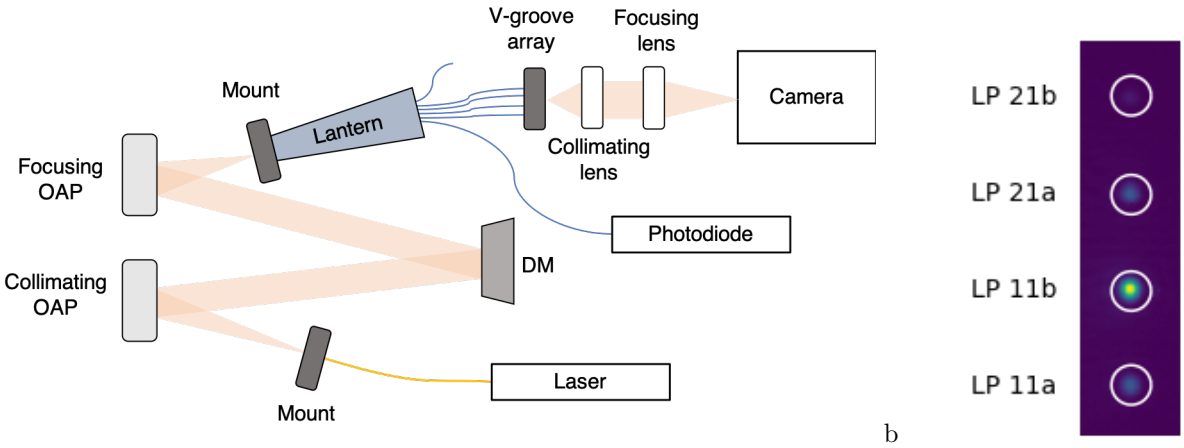

a b

Figure 2. a) A simplified diagram of the experimental setup. A monochromatic 1568.772 nm laser is injected into the bench, and the beam is collimated. A 12×12 deformable mirror can be used to manipulate the wavefront of the beam before it is focused onto the lantern. The SMF outputs of the lantern can then be routed to either a V-groove array to be imaged onto the camera, or to the photodiode. The photodiode is calibrated to a photometer that can slide into the beam just before the lantern, and thus provides measurements normalized to the incoming beam. While performing wavefront control, all four nulled ports are routed to the V-groove. We leave the non-nulled ports disconnected in order to not saturate the camera. After performing wavefront control, we use the photodiode to obtain normalized coupling maps sequentially for each port.

Figure 3a shows an example closed-loop iEFC run where, after the first twenty iterations (using an integration time of 0.2 ms), several of the ports became somewhat faint on the camera. At this point, we increased the exposure time to 0.8 ms to obtain more signal on those ports, and recalculated the response matrix and control matrix. Doing this resulted in closed-loop behavior that drove down the coupling in the LP 21a port at the expense of the other ports, achieving a mean suppression ratio (final η_s divided by initial η_s) of 0.267. Since this was not the desired behavior, we reverted to the DM map at iteration 20 and continued to run iEFC with the original integration time of 0.2 ms and without relinearizing the response matrix. This resulted in most of the ports being driven down, though the LP 21b port rose slightly from its deepest point. Although no port reached a null as deep as the LP 21a port in the first run, the final mean flux was deeper, with mean suppression ratio of 0.156. Additionally, in this case, all ports reached a similar level of coupled flux. Note that because we kept the original integration time, the signal on the camera was very low at this point.

We then obtain normalized coupling maps using the photodiode, both with the original DM map and with the DM map after running iEFC (without relinearization), and present them in Figure 4. These maps were taken on a different day, and because we expected the system have drifted since the end of the iEFC run, we took an additional camera measurement as a reference point, shown in Figure 3b as cross-shaped marks. The difference between the cross-marks and the last measurement of the run indicates the level of system drift over about a day-and-a-half. Interestingly, the system actually drifted to a lower mean coupling (suppression factor of 0.104), with three nulls degrading slightly and one null (spuriously) improving significantly.

The finely-sampled center maps show that the lantern was not perfectly aligned initially, likely because the calculation of the alignment location was performed on full (coarsely-sampled) coupling maps instead of finely-sampled ones of the center. Future work will involve repeating the experiment with better initial calibration and alignment. However, these results show that the algorithm is robust to some degree of initial misalignment, and will in fact correct it if it makes the measured null deeper.

The numerical values of $\eta_{p_{peak}}$ (the peak planet coupling, or the maximum coupling value for each port) and η_s for the four nulled ports before and after performing iEFC are shown in Table 1. Also shown is the suppression factor obtained by using iEFC. The signal on the photodiode is much better than it is on the camera at the end of the run, but the mean suppression factor it measures is 0.110, which is consistent with the mean suppression factor measured on the camera. Meanwhile, the peak planet coupling drops on average by about 20% of the

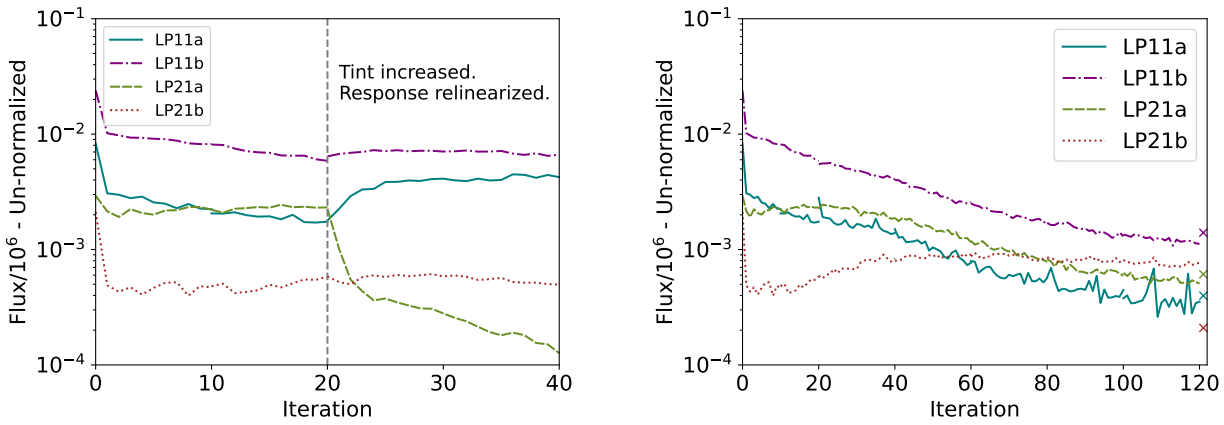

Figure 3. Two example iEFC runs that share the same first twenty iterations. In part a), the integration time was increased and the system relinearized after iteration 20, and the LP 21a port was driven down at the expense of the others, achieving a mean suppression ratio of 0.267. In part b), we continued to run iEFC at the original integration time without relinearizing, and all four ports reached a similar level of suppression, with a mean suppression value of 0.156. The two test runs exhibit very different behavior, indicating that the final result can be strongly influenced by experimental parameters such as changes in integration time or when the system is relinearized. The measurements (on the y-axis) have been divided by 10^6 so that they are at a similar scale to the control inputs, and also scaled appropriately by relative integration time. The cross-shaped marks in part b) indicate the measurement made on the camera just before obtaining normalized coupling maps with the photodiode (shown in Figure 4).

Table 1. The values of $\eta_{p_{peak}}$ (the peak planet coupling, or the maximum coupling value for each port) and η_s for the four nulled ports before and after performing iEFC. Also shown is the suppression factor (final η_s divided by initial η_s) obtained by using iEFC.

	LP 11a	**LP 11b**	**LP 21a**	**LP 21b**
$\eta_{p_{\text{peak}}}$ (Before)	0.408	0.368	0.119	0.111
$\eta_{p_{\text{peak}}}$ (After)	0.355	0.259	0.102	0.089
η_s (Before)	1.74×10^{-2}	3.85×10^{-2}	5.09×10^{-3}	3.38×10^{-3}
η_s (After)	7.89×10^{-4}	3.90×10^{-3}	1.75×10^{-3}	6.54×10^{-4}
iEFC Suppression Factor	0.046	0.101	0.345	0.194

initial value. While this is significant, the improvement in the nulls still results in a better signal-to-noise ratio than not performing wavefront control, whether the noise is expected to be primarily shot noise or systematic noise. A comparison of the stellar coupling and raw contrasts before and after iEFC are also plotted in Figure 5.

5. DISCUSSION AND FUTURE WORK

We have explored the behavior of the iEFC algorithm and shown that it depends heavily on experimental parameters such as when integration times are changed and when the system is relinearized, and can sometimes drive one port to deeper nulls at the expense of other ports. This is undesired behavior, even if the mean coupling of the system is reduced. Future work will involve investigating effective strategies for achieving the desired behavior, such as by finding appropriate weights to apply to each port or by penalizing solutions that degrade the null in any ports. Furthermore, while controling all four nulled ports is useful for a blind search, if the planet location is known, targeting one port for nulling would be more effective, as a deeper null can likely be achieved with less degradation of planet coupling. It is also worth exploring how other experimental parameters affect the performance, such as the number of modes calibrated in the response matrix or the shape of the probes. Ultimately, we have demonstrated that wavefront sensing and control algorithms originally developed

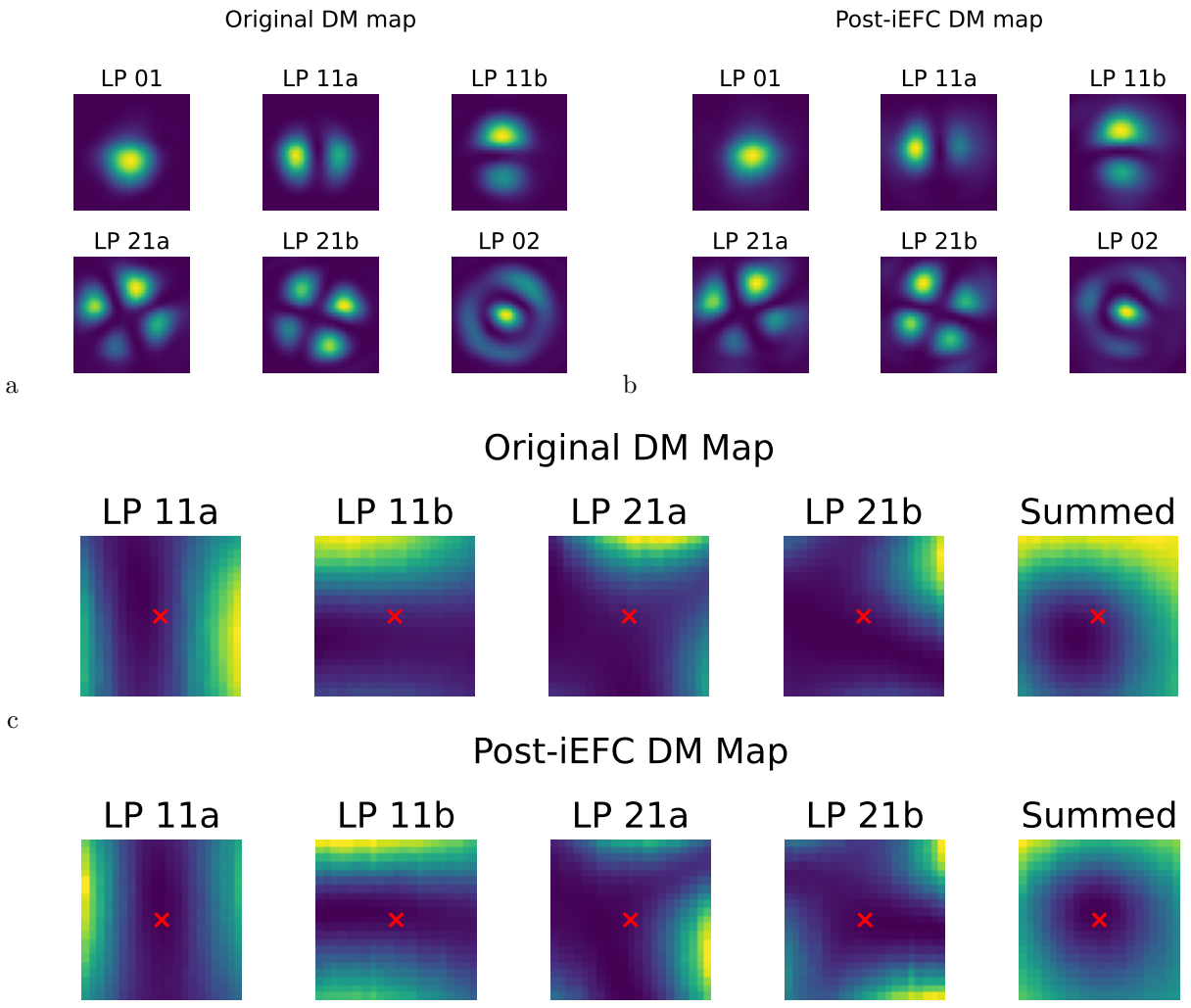

Figure 4. a) The normalized coupling maps using the original DM surface. b) The normalized coupling maps using the DM solution found with iEFC. c) Finely-sampled coupling maps of the lantern center using the original DM surface. d) Finely-sampled coupling maps of the lantern center using the DM solution found with iEFC. The red crosses indicate the location where the beam is aligned for the camera measurements in Figure 3, and also where η_s is measured.

for coronagraphic instruments can also be used to enhance the performance of the PLN, and future work will focus on refining and optimizing the algorithms for use with the PLN.

ACKNOWLEDGMENTS

Y.X acknowledges support from the National Science Foundation Graduate Research Fellowship under Grant No. 1122374. Additional effort has been supported by the National Science Foundation under Grant Nos. 2109231 and 2308360. This research was carried out in part at the California Institute of Technology and the Jet Propulsion Laboratory under a contract with the National Aeronautics and Space Administration (NASA).

This research made use of hcipy;[13] Astropy;[14–16] NumPy;[17] SciPy;[18] and Matplotlib.[19]

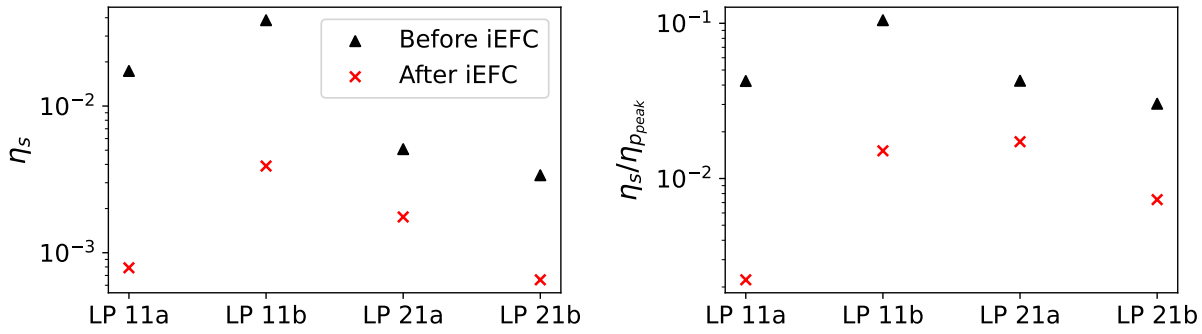

Figure 5. Left) A comparison of the measured stellar coupling (η_s) before and after performing iEFC. Right) A comparison of the raw contrast ($\eta_s/\eta_{p_{peak}}$) before and after performing iEFC. These results show that wavefront control can be used to significantly improve the stellar null with only a slight degradation to the planet coupling, resulting in much higher performance overall for the PLN.

REFERENCES

[1] National Research Council, [*Pathways to Discovery in Astronomy and Astrophysics for the 2020s*], The National Academies Press, Washington, DC (2021).

[2] Wang, J., Mawet, D., Ruane, G., Hu, R., and Benneke, B., "Observing Exoplanets with High Dispersion Coronagraphy. I. The Scientific Potential of Current and Next-generation Large Ground and Space Telescopes," *The Astronomical Journal* **153**, 183 (Apr. 2017).

[3] Ruffio, J.-B., Horstman, K., Mawet, D., Rosenthal, L. J., Batygin, K., Wang, J. J., Millar-Blanchaer, M., Wang, J., Fulton, B. J., Konopacky, Q. M., Agrawal, S., Hirsch, L. A., Howard, A. W., Blunt, S., Nielsen, E., Baker, A., Bartos, R., Bond, C. Z., Calvin, B., Cetre, S., Delorme, J.-R., Doppmann, G., Echeverri, D., Finnerty, L., Fitzgerald, M. P., Jovanovic, N., López, R., Martin, E. C., Morris, E., Pezzato, J., Ruane, G., Sappey, B., Schofield, T., Skemer, A., Venenciano, T., Wallace, J. K., Wallack, N. L., Wizinowich, P., and Xuan, J. W., "Detecting Exomoons from Radial Velocity Measurements of Self-luminous Planets: Application to Observations of HR 7672 B and Future Prospects," *The Astronomical Journal* **165**, 113 (Mar. 2023).

[4] Xin, Y., Jovanovic, N., Ruane, G., Mawet, D., Fitzgerald, M. P., Echeverri, D., Lin, J., Leon-Saval, S., Gatkine, P., Kim, Y. J., Norris, B., and Sallum, S., "Efficient Detection and Characterization of Exoplanets within the Diffraction Limit: Nulling with a Mode-selective Photonic Lantern," **938**, 140 (Oct. 2022).

[5] Tuthill, P., "Nulling interferometry: high contrast science for single large apertures," in [*Adaptive Optics Systems VIII*], Schreiber, L., Schmidt, D., and Vernet, E., eds., **12185**, 121858P, International Society for Optics and Photonics, SPIE (2022).

[6] Ruane, G., Wang, J., Mawet, D., et al., "Efficient spectroscopy of exoplanets at small angular separations with vortex fiber nulling," *Astrophys. J.* (2018).

[7] Echeverri, D., Ruane, G., Jovanovic, N., Mawet, D., and Levraud, N., "Vortex fiber nulling for exoplanet observations I Experimental demonstration in monochromatic light," *Optics Letters* **44**, 2204 (May 2019).

[8] Leon-Saval, S. G., Fontaine, N. K., Salazar-Gil, J. R., Ercan, B., Ryf, R., and Bland-Hawthorn, J., "Mode-selective photonic lanterns for space-division multiplexing," *Opt. Express* **22**, 1036–1044 (Jan 2014).

[9] Leon-Saval, S. G., Argyros, A., and Bland-Hawthorn, J., "Photonic lanterns," *Nanophotonics* **2**, 429–440 (Dec. 2013).

[10] Xin, Y., Echeverri, D., Jovanovic, N., Mawet, D., Leon-Saval, S., Amezcua-Correa, R., Yerolatsitis, S., Fitzgerald, M. P., Gatkine, P., Kim, Y. J., Lin, J., Norris, B., Ruane, G., and Sallum, S., "Laboratory demonstration of a Photonic Lantern Nuller in monochromatic and broadband light," *Journal of Astronomical Telescopes, Instruments, and Systems* **10**(2), 025001 (2024).

[11] Haffert, S. Y., Males, J. R., Ahn, K., Van Gorkom, K., Guyon, O., Close, L. M., Long, J. D., Hedglen, A. D., Schatz, L., Kautz, M., Lumbres, J., Rodack, A., Knight, J. M., and Miller, K., "Implicit electric field conjugation: Data-driven focal plane control," **673**, A28 (May 2023).

[12] Milani, K., Derby, K., and Douglas, E., "lina (v0.1)." https://doi.org/10.5281/zenodo.11195112.

[13] Por, E. H., Haffert, S. Y., Radhakrishnan, V. M., Doelman, D. S., Van Kooten, M., and Bos, S. P., "High Contrast Imaging for Python (HCIPy): an open-source adaptive optics and coronagraph simulator," in [*Adaptive Optics Systems VI*], *Proc. SPIE* **10703** (2018).

[14] Astropy Collaboration, Robitaille, T. P., Tollerud, E. J., Greenfield, P., Droettboom, M., Bray, E., Aldcroft, T., Davis, M., Ginsburg, A., Price-Whelan, A. M., Kerzendorf, W. E., Conley, A., Crighton, N., Barbary, K., Muna, D., Ferguson, H., Grollier, F., Parikh, M. M., Nair, P. H., Unther, H. M., Deil, C., Woillez, J., Conseil, S., Kramer, R., Turner, J. E. H., Singer, L., Fox, R., Weaver, B. A., Zabalza, V., Edwards, Z. I., Azalee Bostroem, K., Burke, D. J., Casey, A. R., Crawford, S. M., Dencheva, N., Ely, J., Jenness, T., Labrie, K., Lim, P. L., Pierfederici, F., Pontzen, A., Ptak, A., Refsdal, B., Servillat, M., and Streicher, O., "Astropy: A community Python package for astronomy," *Astronomy and Astrophysics* **558**, A33 (Oct. 2013).

[15] Price-Whelan, A. M., Sipőcz, B. M., Günther, H. M., Lim, P. L., Crawford, S. M., Conseil, S., Shupe, D. L., Craig, M. W., Dencheva, N., Ginsburg, A., VanderPlas, J. T., Bradley, L. D., Pérez-Suárez, D., de Val-Borro, M., Paper Contributors, P., Aldcroft, T. L., Cruz, K. L., Robitaille, T. P., Tollerud, E. J., Coordination Committee, A., Ardelean, C., Babej, T., Bach, Y. P., Bachetti, M., Bakanov, A. V., Bamford, S. P., Barentsen, G., Barmby, P., Baumbach, A., Berry, K. L., Biscani, F., Boquien, M., Bostroem, K. A., Bouma, L. G., Brammer, G. B., Bray, E. M., Breytenbach, H., Buddelmeijer, H., Burke, D. J., Calderone, G., Cano Rodríguez, J. L., Cara, M., Cardoso, J. V. M., Cheedella, S., Copin, Y., Corrales, L., Crichton, D., D'Avella, D., Deil, C., Depagne, É., Dietrich, J. P., Donath, A., Droettboom, M., Earl, N., Erben, T., Fabbro, S., Ferreira, L. A., Finethy, T., Fox, R. T., Garrison, L. H., Gibbons, S. L. J., Goldstein, D. A., Gommers, R., Greco, J. P., Greenfield, P., Groener, A. M., Grollier, F., Hagen, A., Hirst, P., Homeier, D., Horton, A. J., Hosseinzadeh, G., Hu, L., Hunkeler, J. S., Ivezić, Ž., Jain, A., Jenness, T., Kanarek, G., Kendrew, S., Kern, N. S., Kerzendorf, W. E., Khvalko, A., King, J., Kirkby, D., Kulkarni, A. M., Kumar, A., Lee, A., Lenz, D., Littlefair, S. P., Ma, Z., Macleod, D. M., Mastropietro, M., McCully, C., Montagnac, S., Morris, B. M., Mueller, M., Mumford, S. J., Muna, D., Murphy, N. A., Nelson, S., Nguyen, G. H., Ninan, J. P., Nöthe, M., Ogaz, S., Oh, S., Parejko, J. K., Parley, N., Pascual, S., Patil, R., Patil, A. A., Plunkett, A. L., Prochaska, J. X., Rastogi, T., Reddy Janga, V., Sabater, J., Sakurikar, P., Seifert, M., Sherbert, L. E., Sherwood-Taylor, H., Shih, A. Y., Sick, J., Silbiger, M. T., Singanamalla, S., Singer, L. P., Sladen, P. H., Sooley, K. A., Sornarajah, S., Streicher, O., Teuben, P., Thomas, S. W., Tremblay, G. R., Turner, J. E. H., Terrón, V., van Kerkwijk, M. H., de la Vega, A., Watkins, L. L., Weaver, B. A., Whitmore, J. B., Woillez, J., Zabalza, V., and Contributors, A., "The Astropy Project: Building an Open-science Project and Status of the v2.0 Core Package," *Astronomical Journal* **156**, 123 (Sept. 2018).

[16] Astropy Collaboration, Price-Whelan, A. M., Lim, P. L., Earl, N., Starkman, N., Bradley, L., Shupe, D. L., Patil, A. A., Corrales, L., Brasseur, C. E., Nöthe, M., Donath, A., Tollerud, E., Morris, B. M., Ginsburg, A., Vaher, E., Weaver, B. A., Tocknell, J., Jamieson, W., van Kerkwijk, M. H., Robitaille, T. P., Merry, B., Bachetti, M., Günther, H. M., Aldcroft, T. L., Alvarado-Montes, J. A., Archibald, A. M., Bódi, A., Bapat, S., Barentsen, G., Bazán, J., Biswas, M., Boquien, M., Burke, D. J., Cara, D., Cara, M., Conroy, K. E., Conseil, S., Craig, M. W., Cross, R. M., Cruz, K. L., D'Eugenio, F., Dencheva, N., Devillepoix, H. A. R., Dietrich, J. P., Eigenbrot, A. D., Erben, T., Ferreira, L., Foreman-Mackey, D., Fox, R., Freij, N., Garg, S., Geda, R., Glattly, L., Gondhalekar, Y., Gordon, K. D., Grant, D., Greenfield, P., Groener, A. M., Guest, S., Gurovich, S., Handberg, R., Hart, A., Hatfield-Dodds, Z., Homeier, D., Hosseinzadeh, G., Jenness, T., Jones, C. K., Joseph, P., Kalmbach, J. B., Karamehmetoglu, E., Kałuszyński, M., Kelley, M. S. P., Kern, N., Kerzendorf, W. E., Koch, E. W., Kulumani, S., Lee, A., Ly, C., Ma, Z., MacBride, C., Maljaars, J. M., Muna, D., Murphy, N. A., Norman, H., O'Steen, R., Oman, K. A., Pacifici, C., Pascual, S., Pascual-Granado, J., Patil, R. R., Perren, G. I., Pickering, T. E., Rastogi, T., Roulston, B. R., Ryan, D. F., Rykoff, E. S., Sabater, J., Sakurikar, P., Salgado, J., Sanghi, A., Saunders, N., Savchenko, V., Schwardt, L., Seifert-Eckert, M., Shih, A. Y., Jain, A. S., Shukla, G., Sick, J., Simpson, C., Singanamalla, S., Singer, L. P., Singhal, J., Sinha, M., Sipőcz, B. M., Spitler, L. R., Stansby, D., Streicher, O., Šumak, J., Swinbank,

J. D., Taranu, D. S., Tewary, N., Tremblay, G. R., de Val-Borro, M., Van Kooten, S. J., Vasović, Z., Verma, S., de Miranda Cardoso, J. V., Williams, P. K. G., Wilson, T. J., Winkel, B., Wood-Vasey, W. M., Xue, R., Yoachim, P., Zhang, C., Zonca, A., and Astropy Project Contributors, "The Astropy Project: Sustaining and Growing a Community-oriented Open-source Project and the Latest Major Release (v5.0) of the Core Package," **935**, 167 (Aug. 2022).

[17] Harris, C. R., Millman, K. J., van der Walt, S. J., Gommers, R., Virtanen, P., Cournapeau, D., Wieser, E., Taylor, J., Berg, S., Smith, N. J., Kern, R., Picus, M., Hoyer, S., van Kerkwijk, M. H., Brett, M., Haldane, A., del Río, J. F., Wiebe, M., Peterson, P., Gérard-Marchant, P., Sheppard, K., Reddy, T., Weckesser, W., Abbasi, H., Gohlke, C., and Oliphant, T. E., "Array programming with NumPy," *Nature* **585**, 357–362 (Sept. 2020).

[18] Virtanen, P., Gommers, R., Oliphant, T. E., Haberland, M., Reddy, T., Cournapeau, D., Burovski, E., Peterson, P., Weckesser, W., Bright, J., van der Walt, S. J., Brett, M., Wilson, J., Jarrod Millman, K., Mayorov, N., Nelson, A. R. J., Jones, E., Kern, R., Larson, E., Carey, C., Polat, İ., Feng, Y., Moore, E. W., Vand erPlas, J., Laxalde, D., Perktold, J., Cimrman, R., Henriksen, I., Quintero, E. A., Harris, C. R., Archibald, A. M., Ribeiro, A. H., Pedregosa, F., van Mulbregt, P., and Contributors, S. . ., "SciPy 1.0: Fundamental Algorithms for Scientific Computing in Python," *Nature Methods* **17**, 261–272 (2020).

[19] Hunter, J. D., "Matplotlib: A 2D graphics environment," *Computing in Science & Engineering* **9**(3), 90–95 (2007).